150
4/27/87 JEM

⑤

DR 0225-9
I-30297

ORNL/TM-10331

ornl

OAK RIDGE
NATIONAL
LABORATORY

MARTIN MARIETTA

Stability of Ideal and Resistive Internal Kink Modes in Toroidal Geometry

R. J. Hastie
T. C. Hender
B. A. Carreras
L. A. Charlton
J. A. Holmes

OPERATED BY
MARTIN MARIETTA ENERGY SYSTEMS, INC.
FOR THE UNITED STATES
DEPARTMENT OF ENERGY

ORNL/TM--10331

DE87 008565

Fusion Energy Division

STABILITY OF IDEAL AND RESISTIVE INTERNAL KINK MODES IN TOROIDAL GEOMETRY

R. J. Hastie
T. C. Hender
Culham Laboratory, Abingdon, Oxfordshire
(EURATOM/UKAEA Fusion Association)

B. A. Carreras
Fusion Energy Division
Oak Ridge National Laboratory

L. A. Charlton
J. A. Holmes
Computing and Telecommunications Division
Martin Marietta Energy Systems, Inc.

DATE PUBLISHED — February 1987

NOTICE: This document contains information of a preliminary nature. It is subject to revision or correction and therefore does not represent a final report.

Prepared by the
OAK RIDGE NATIONAL LABORATORY
Oak Ridge, Tennessee 37831
operated by
MARTIN MARIETTA ENERGY SYSTEMS, INC.
for the
U.S. DEPARTMENT OF ENERGY
under contract DE-AC0[illegible]-84OR21400

DISTRIBUTION OF THIS DOCUMENT IS UNLIMITED

MASTER

CONTENTS

ACKNOWLEDGMENTS

T. C. Hender was supported in part by a task agreement between the JET Joint Undertaking and Culham Laboratory.

ABSTRACT

The stability of the ideal and resistive $m = 1$ internal modes is investigated for tokamak equilibria having a variety of different $q(r)$ profiles, including non-monotonic $q(r)$ with multiple $q = 1$ surfaces. Detailed comparisons between analytic theory and numerical results from a linear toroidal MHD code are presented. Particular attention is paid to the study of equilibria near marginal stability.

1. INTRODUCTION

Theoretical investigations of the internal disruptions (sawtooth behavior) observed in most tokamak discharges have concentrated on three separate aspects of the phenomenon:

1. the reconnection occurring[1–6] during the nonlinear phase of the $m = 1$, $n = 1$ kink instability,
2. the simulation by transport codes[3,4] of the slow evolution of the discharge that returns it to a kink-unstable state, resulting in the cyclic behavior observed,
3. the establishment of marginal stability criteria for the internal kink mode (resistive as well as ideal) and studies of linear growth[7–12] near to marginal stability.

Without the third ingredient, the transport simulations lack credibility because they assume that the plasma reconnects when some arbitrary criterion is satisfied, and the nonlinear reconnection studies lack credibility because they start from a strongly unstable equilibrium.

Recent sawtooth simulations[13,14] have employed reduced fluid equations that follow both the fast Alfvénic time scales and the transport time scale. The equations include electron thermal transport both along and across the magnetic field, as well as resistivity. These simulations extend the earlier work of Sykes and Wesson[5] and have been very successful in producing cyclical reconnecting behavior. However, the geometry is cylindrical, and the stability properties of the internal kink mode are quite different in cylindrical and toroidal geometry.[8] The conditions under which each thermal collapse is triggered may therefore be rather different in this simulation from those holding in a real tokamak discharge.

Another difficulty encountered in sawtooth simulations concerns the very fast collapse time frequently observed in large tokamaks (100 μs in JET). As noted by Wesson,[7] this collapse time is at variance with the estimate given by Kadomtsev, and it is difficult to reconcile with any mechanism involving a transport-induced evolution through a linear stability boundary, be it of an ideal or a resistive mode. If such a mechanism is responsible for the temperature collapse, an exceedingly sharp stability boundary must be involved: sharp, that is, in the sense of large growth rates being possible for equilibrium parameters close to marginality.

A knowledge of linear stability criteria and linear growth rates near marginal stability is therefore an important ingredient in understanding sawtoothing in tokamaks. An important contribution in this field is the toroidal calculation of the ideal MHD energy δW by Bussac et al.[8] (subsequently presented in more detail in refs. 15–17). From a later paper by Bussac et al.,[10] one can obtain analytic expressions for the linear growth rate of the internal kink mode in a resistive plasma as well as in the ideal limit $S \to \infty$ (where S is the magnetic Reynolds number). These results are limited in several ways, all of which may be relevant to understanding sawtoothing.

1. The analysis assumes an aspect ratio expansion of the equilibrium, and orders $\beta \sim \epsilon^2$, where ϵ is the inverse aspect ratio.
2. Only $q(r)$ profiles (where q is the safety factor) having a single $q = 1$ radius are considered.
3. In the inner region, $r \leq r_1$, where $q(r_1) = 1$, the ordering $|q - 1| \gg \epsilon$ is assumed.

It is the purpose of this paper to remove these limitations and to establish the internal kink stability properties of tokamaks for a variety of $q(r)$ profiles, including nonmonotonic $q(r)$, at finite as well as large aspect ratio. We devote particular attention to identifying marginally stable equilibrium configurations and to evaluating growth rates close to marginality, for both the ideal and resistive internal kink modes. Detailed quantitative comparisons are made between the computational results obtained from a linear toroidal resistive MHD code (FAR)[18,19] and analytic results.

The structure of the paper is as follows. Section 2 summarizes the analytic theory for ideal internal kink modes when a single $q = 1$ surface is present in the plasma and extends it to cases for which two $q = 1$ radii are present. In Sect. 3, results from analytic theory are compared with numerical growth rates obtained from the FAR code. Section 4 presents numerical results for tight-aspect-ratio devices, strong shaping, and very low shear profiles. These calculations include examples that model the measured q profiles in ASDEX[20] and in TEXTOR.[21] Many of the calculations are for equilibria consistent with JET. These cases are strictly beyond the regime of validity of the analytic theories. Section 5 summarizes the results, and conclusions on the nature of the sawtooth collapse are drawn.

2. ANALYTIC THEORY OF INTERNAL KINK STABILITY

2.1 CASES WITH A SINGLE *q=1* SURFACE

The ideal MHD toroidal stability problem was considered for a large-aspect-ratio torus by Bussac et al.,[8] and the effect of shaping was analyzed by Edery et al.[22] Shaping effects decouple from toroidal effects in the large-aspect-ratio limit, so that the combined effects are additive. For an equilibrium of circular cross section, the energy integral δW, after minimization, is given by

$$\delta W = 2\pi^2 R B_0^2 \, |\xi|^2 \, \frac{r_1^4}{R^2} \, \delta W^T \ , \tag{1}$$

where

$$\begin{aligned}\delta W^T = \Big[& 8s(b-c) + \frac{9}{4}(b-1)(1-c) - 6(b-1)(c+3)(\beta_p + s) \\ & -4(c+3)(b+3)(\beta_p + s)^2 \Big] \times [16(b-c)]^{-1} \ ,\end{aligned} \tag{2}$$

$$s = \int_0^{r_1} \frac{dr}{r_1} \left(\frac{r}{r_1}\right)^3 \left(\frac{1}{q^2} - 1\right) \ , \tag{3}$$

$$\beta_p = -\frac{2}{B_p^2(r_1)} \int_0^{r_1} \frac{dp}{dr} \left(\frac{r}{r_1}\right)^2 dr \ , \tag{4}$$

with B_p the poloidal field strength and r_1 the radius at which $q(r) = 1$. The quantities b and c in δW^T are the values of the logarithmic derivatives

$$b = \frac{r_1}{\xi} \frac{d\xi}{dr}\bigg|_{r_1 -} \quad ; \quad c = \frac{r_1}{\xi} \frac{d\xi}{dr}\bigg|_{r_1 +} \ , \tag{5}$$

obtained by integrating the $m = 2$ Euler equation,

$$\frac{d}{dr}\left[r^3 \left(\frac{1}{q} - \frac{1}{m}\right)^2 \frac{d\xi}{dr}\right] - (m^2 - 1)\left(\frac{1}{q} - \frac{1}{m}\right)^2 r\xi = 0 \ , \tag{6}$$

from the axis (with regular boundary conditions there) to give b and from the $q = 2$ surface (or the plasma boundary, if there is no $q = 2$ surface within the plasma) to give c.

An important consequence of the toroidal geometry[8] is that the cylindrical contribution to δW is identically cancelled out for an $n = 1$, $m = 1$ mode. It follows that if the value of the ideal MHD energy, δW, is important in determining the trigger for internal disruption and reconnection, cylindrical simulations must give incorrect results.

To obtain the linear growth rate of either the ideal MHD mode or the resistive kink mode, the calculation of δW must be supplemented by a theory of the singular layer.

In the case of the ideal mode, the growth rate may be obtained by equating the kinetic energy,

$$K = \frac{\gamma^2}{2} \rho \int |\xi|^2 \, d^3x \, , \tag{7}$$

to the potential energy available for instability, $(-\delta W)$.[23] Because of the inertial layer at r_1, K is dominated by the contributions from ξ_θ^2 and ξ_ϕ^2 in the inertial layer, where

$$\begin{aligned} \xi_\theta &\sim -i \frac{d\xi_r}{dr} \\ \xi_\phi &\sim 2 \sin\theta \frac{d\xi_r}{dr} \, , \end{aligned} \tag{8}$$

while the discontinuity at the singular layer is resolved by the inertia, and one finds

$$\frac{d}{dr} \left\{ \left[3\frac{\gamma^2}{\omega_A^2} + \left(\frac{1}{q} - 1 \right)^2 \right] \frac{d\xi_r}{dr} \right\} = 0 \, , \tag{9}$$

with $\omega_A = V_A/R$ and V_A the Alfvén velocity.

The factor 3 appearing in Eq. (9) is the inertial enhancement factor $M \simeq 1 + 2q^2$ found by Glasser, Greene, and Johnson[24] in toroidal geometry. To obtain the correct linear growth, one must add the field line bending modification to the potential energy that comes from the layer. This is given by

$$\delta\overline{W} = \frac{1}{2} \int d^3x B_0^2 \left(\frac{1}{q} - 1 \right)^2 \left| \frac{d\xi_r}{dr} \right|^2 \, . \tag{10}$$

At marginal stability this contribution vanishes; however, when Eq. (9) is used to give the layer solution, a finite contribution is obtained.

Finally, equating $K = -\left(\delta W + \delta \overline{W}\right)$, one obtains the linear growth rate

$$\left[\int_{-\infty}^{\infty} \frac{dx}{3\left(\gamma^2/\omega_A^2\right) + (q-1)^2}\right]^{-1} = -\frac{r_1^2}{R^2}\,\delta W^T \,, \tag{11}$$

where $x = (r - r_1)/r_1$ is the local radial variable.

Several cases can now be distinguished.

1. Monotonic $q(r)$, with $q(r_1) = 1$ and $q'(r_1) \neq 0$ (solid line in Fig. 1),

$$\frac{\gamma}{\omega_A} = \frac{1}{r_1 q'}\,\frac{\pi}{\sqrt{3}}\left(-\delta W^T\right)\frac{r_1^2}{R^2} \,. \tag{12}$$

2. Nonmonotonic $q(r)$, with a minimum at r_1, $q(r_1) = 1$ and $q'(r_1) = 0$ (dashed line in Fig. 1),

$$\frac{\gamma}{\omega_A} = \frac{\pi^{2/3}}{\sqrt{3}}\,\frac{1}{\left(r_1^2 q''\right)^{1/3}}\left(-\frac{r_1^2}{R^2}\,\delta W^T\right)^{2/3} \,. \tag{13}$$

3. Nonmonotonic $q(r)$, with $q(r_1) \neq 1$ and $q'(r_1) = 0$ (dot-dashed line in Fig. 1),

$$\overline{\gamma}\left(1 + \frac{\delta q}{\overline{\gamma}}\right)^{1/3} = \frac{1}{\left(r_1^2 q''\right)^{1/3}}\left(-\pi\frac{r_1^2}{R^2}\,\delta W^T\right)^{2/3} \,, \tag{14}$$

where $\overline{\gamma} = \left[3\gamma^2/\omega_A^2 + (\delta q)^2\right]^{1/2}$ and $\delta q = q(r_1) - 1 \ll 1$. Equation (14) is valid for both positive and negative values of δq, provided that when $\delta q < 0$, $|\delta q|$ does not become large enough for the inertial layer to separate into two layers at the different $q = 1$ radii. For positive δq, there is a strong stabilizing effect from the field line bending at r_1, and an equilibrium that is unstable when $q_{\min} = 1$ (i.e., for which δW^T is negative) is marginally stable for

$$\delta q = \frac{1}{2^{1/3}}\,\frac{1}{\left(r_1^2 q''\right)^{1/3}}\left(-\pi\frac{r_1^2}{R^2}\,\delta W^T\right)^{2/3} \,. \tag{15}$$

The ideal growth rate peaks for negative δq at $\gamma_{\max} = 1.09\gamma_0$, with γ_0 the $\delta q = 0$ growth rate. As δq becomes more negative, the growth rate decreases, but the single-layer theory eventually becomes invalid. These analytic results are compared with computed growth rates in the next section.

4. Monotonic $q(r)$, with a point of inflection at r_1, $q(r_1) = 1$ and $q'(r_1) = q''(r_1) = 0$,

$$\frac{\gamma}{\omega_A} = \frac{1}{\sqrt{3}}\left(\frac{6}{r_1^3 q'''}\right)^{1/5}\left(-\frac{2\pi}{3}\,\frac{r_1^2}{R^2}\,\delta W^T\right)^{3/5} \,. \tag{16}$$

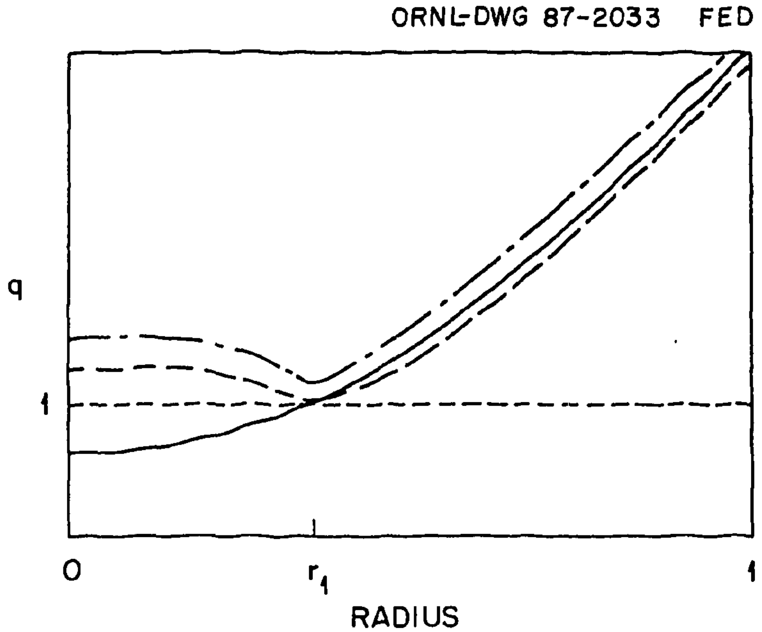

Fig. 1. Profiles of the safety factor $q(r)$ for which ideal MHD growth rates are calculated in Eqs. (12) (solid line), (13) (dashed line), and (14) (dot-dashed line).

The presence of a point of inflection of q at r_1, therefore, enhances the ideal MHD growth rate $\left[\gamma\alpha\left(r_1/R\right)^{6/5}\right]$ when $\delta W^T < 0$. For $\delta W^T > 0$ the resistive stability of such $q(r)$ profiles is investigated in Sect. 4.

2.2 THE ROLE OF RESISTIVITY

In the foregoing estimates of growth rates, it has been assumed that $\delta W^T < 0$, that is, that energy is available to drive the ideal MHD instability. However, even when this is the case, it does not follow that the ideal growth rates calculated above are correct. Resistivity may dominate the layer behavior. To estimate the magnitude of resistive effects, we compare the inductive contribution to the parallel electric field, $\gamma A_{\|}$, with the resistive term in the layer $\eta j_{\|} \propto \eta c^2 A_{\|}/d^2$, where d is a measure of the layer width.

From this we find that resistivity is negligible if the condition

$$\left(\frac{\gamma}{\omega_A}\right)\left(\frac{d^2}{r_1^2}\right) > S^{-1} \tag{17}$$

is satisfied.

Here, $S = \omega_A \tau_r$ with $\tau_r = \eta c^2 / r_1^2$, and a is the minor radius of the device.

Estimating the layer width d from Eq. (9) and the growth rates from Eqs. (12) and (13), we find that for $q'(r_1) \neq 0$, Eq. (17) becomes

$$S^{-1} < \frac{\pi^3}{\sqrt{3}} \left[r_1 q'(r_1)\right]^{-5} \left(\frac{r_1}{R}\right)^6 \left(-\delta W^T\right)^3 \,, \tag{18}$$

while for the nonmonotonic case, with $q_{\text{min}} = 1$, it becomes

$$S^{-1} < \pi^{4/3} \sqrt{4/3}\, \left[r_1^2 q''(r_1)\right]^{-5/3} \left(\frac{r_1}{R}\right)^{8/3} \left(-\delta W^T\right)^{4/3} \,, \tag{19}$$

where the layer width is

$$d/r_1 \simeq \sqrt{2\pi}^{1/3} \left(\frac{r_1}{R} \frac{1}{r_1^2 q''}\right)^{2/3} \left(-\delta W^T\right)^{1/3} \,.$$

Inequality (18) gives the familiar result that resistivity (even with S in the range from 10^6 to 10^8) tends to dominate the linear growth of $m = 1$ modes. Inequality (19), however, shows that because of the broader inertial layer and larger ideal growth rate, the internal kink becomes an essentially ideal mode when the shear vanishes at the $q = 1$ surface.

When $\delta W^T > 0$, no ideal instability is possible and a resistive layer theory is required. Coppi et al.[9] have given this theory in cylindrical geometry (with $q'(r_1) \neq 0$) and Bussac et al.[10] have extended this to toroidal geometry. The dispersion relation is given in ref. 10 with diamagnetic and toroidal coupling effects included. In single-fluid resistive theory, neglecting coupling to the $q = 2$ tearing mode, it reduces to

$$\frac{r_1^2}{R^2} \delta W^T + \frac{2}{\pi} \left(r_1 q'\right)^{3/2} \left(\frac{3\gamma}{\omega_A S}\right)^{1/4} \frac{\mu - 1}{\mu} \frac{\Gamma\left[(\mu + 5)/4\right]}{\Gamma\left[(\mu + 3)/4\right]} = 0 \,, \tag{20}$$

with

$$\mu = \frac{\sqrt{3}}{r q'} \left(\frac{\gamma}{\omega_A}\right)^{3/2} S^{1/2} \,.$$

This yields the ideal MHD growth rate when $\delta W^T < 0$ and $S \to \infty$, and the familiar $\gamma \propto S^{-1/3}$ scaling when

$$S < \left| \frac{r_1^2}{R^2} \delta W^T \right|^3 .$$

For very large S, very tight aspect ratio, or small shear $[q'(r_1) \to 0]$, the scaling of γ is modified to the $S^{-3/5}$ of conventional tearing modes. No theory of the resistive layer appears to have been done when $q'(r_1) = 0$, but, as we shall see from the numerical results, no unstable $m = 1$ resistive mode is found when $q(r) \geq 1$ everywhere, provided the rippling modes are excluded.

2.3 EQUILIBRIA WITH TWO $q=1$ SURFACES

The analytic estimate of the growth rate given by Eq. (14) breaks down when the characteristic layer width d becomes less than the separation of the two $q = 1$ radii when $q_{\min} < 1$.

The analytic minimization of δW for two $q = 1$ radii is similar to the original analysis of Bussac et al. The analysis is outlined in the appendix, where the following expression for δW is obtained:

$$\begin{aligned} \delta W = 2\pi^2 R B_0^2 \Big[& (\xi - \bar{\xi})^2 \frac{r_1^4}{R^2} \delta W_1 + \bar{\xi}^2 \frac{r_2^4}{R^2} \delta W_2 \\ & + \bar{\xi} (\xi - \bar{\xi}) \frac{r_1^4}{R^2} \delta W_3 \Big] , \end{aligned} \tag{21}$$

with r_1 the radius of the first and r_2 the radius of the second $q = 1$ surface, ξ the amplitude of the "top hat" $m = 1$ eigenfunction in $[0, r_1]$, and $\bar{\xi}$ the amplitude in $[r_1, r_2]$. The expressions for δW_1, δW_2, and δW_3 are given in the appendix. They depend on the quantities

$$s_j = \int_0^{r_j} \frac{dr}{r_j} \left(\frac{r}{r_j} \right)^3 \left(\frac{1}{q^2} - 1 \right) , \quad j = 1,2 \tag{22}$$

and

$$\beta_{pj} = -\frac{2}{B_p^2(r_j)} \int_0^{r_j} \frac{dp}{dr} \left(\frac{r}{r_j} \right)^2 dr , \quad j = 1,2 , \tag{23}$$

which are obvious generalizations of the single-surface case.

The ideal growth rates and eigenfunctions (ratio of ξ to $\overline{\xi}$) of the two possible ideal modes are also calculated in the appendix. The results are

$$\frac{\gamma}{\omega_A} = \frac{\pi}{\sqrt{3}}\frac{1}{2DE}\left[(AE+CD) \pm \sqrt{(AE+CD)^2+(B^2-4AC)DE}\right] \tag{24}$$

and

$$\xi/\overline{\xi} = 1 + \frac{r_2}{r_1}\frac{1}{BE}\left[-(AE-CD) \pm \sqrt{(AE+CD)^2+(B^2-4AC)DE}\right] , \tag{25}$$

where

$$A = \frac{r_2^2}{R^2}\,\delta W_2, \quad B = \frac{r_1^3}{R^2 r_2}\,\delta W_3, \quad C = \frac{r_1^2}{R^2}\,\delta W_1, \quad D = |r_2 q'(r_2)|, \quad E = |r_1 q'(r_1)| \ .$$

3. COMPARISON OF ANALYTIC AND NUMERICAL RESULTS

In this section we demonstrate the very close agreement between the aspect ratio expansion analytic techniques presented in Sect. 2 and computational results obtained using a modified version of the FAR code.[18] The modified FAR code[19] solves the linear compressible (or incompressible) resistive MHD equations in full toroidal geometry, with no ordering assumptions. The double equations of state, $dp/dt = 0$ and $\nabla \cdot \left(\underline{v}/R^2\right) = 0$, employed in the original FAR code[18] have therefore been replaced by the adiabatic equation of state or, in the incompressible case, by $\nabla \cdot \underline{v} = 0$. As a result, the localized resistive-pressure-driven modes that appeared in earlier $m = 1$ simulations using the original FAR code,[18] and in simulations with reduced equations using the RST code,[25] do not appear at finite beta.

In all other respects, the new version of FAR is identical to the original code as described in ref. 18. As input to the FAR code, the flux coordinates are computed from numerical solution of the Grad-Shafranov equation.

3.1 MONOTONIC $q(r)$

Figure 2 shows the variation of ideal MHD growth rate with beta for monotonic $q(r) = 0.9\left(1 + r^2\right)$. The aspect ratio $A = 10^2$, and the pressure profile is a parabolic function of r, the flux coordinate used in ref. 8. For this comparison the logarithmic derivatives b and c of Eq. (5) were evaluated numerically and found to be 1.15 and -2.02, respectively. The code was run incompressibly with resistivity set to zero. As predicted analytically, $\gamma \propto \beta^2$, and close agreement exists between computational and analytic results.

Figure 3 shows the growth rate of the resistive mode as a function of the magnetic Reynolds number S for the equilibrium of Fig. 2, but at zero beta. The comparison is now with the analytic prediction taken from Eq. (20). Within the range of S values investigated, the dispersion relation is effectively $\mu = 1$, so that δW^T plays no role. The growth rate scales as $S^{-1/3}$. At even higher S, a transition to $S^{-3/5}$ behavior should occur (probably beyond $S = 10^{12}$ for this case). This transition is demonstrated for an equilibrium of tight aspect ratio in Sect. 4.

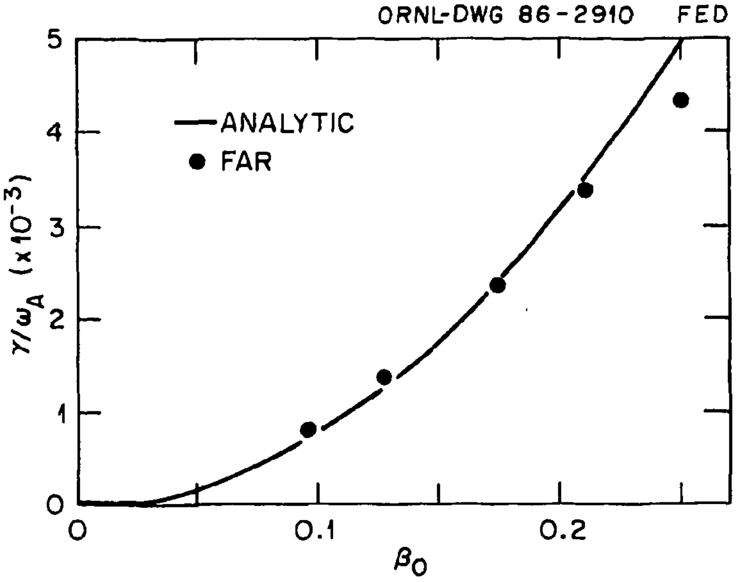

Fig. 2. Comparison of analytic [Eq. (12)] and computed growth rates for the ideal MHD mode, as functions of peak $\beta_0 = 2p(0)/B_0^2$. $A = 10^2$, $q(r) = 0.9(1 + r^2)$, $p(r) = p_0(1 - r^2)$.

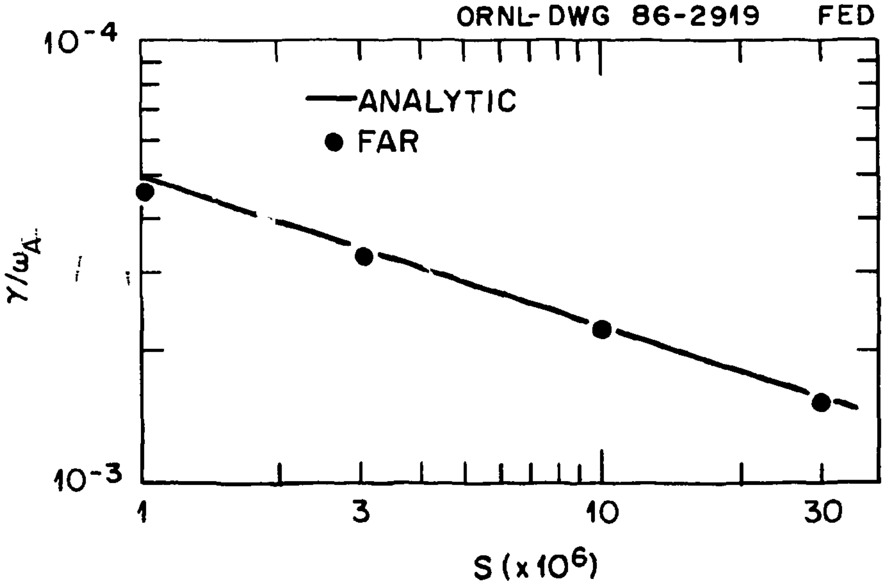

Fig. 3. Comparison of analytic [Eq. (20)] and computed growth rates for the resistive kink instability, as functions of magnetic Reynolds number S. $A = 10^2$, $\beta_0 = 0$, $q = 0.9(1 + r^2)$.

3.2 NONMONOTONIC $q(r)$

In Fig. 4 we compare the ideal MHD growth rates computed from the FAR code with those calculated analytically for the nonmonotonic profile,

$$q = q_{\min} + 0.2\left(1 - 4r^2\right)^2 \ ,$$

at zero beta and $A = 10$.

The solid curve is that given by Eq. (24), which should be valid whenever two separate inertial layers are present. The dashed curve is evaluated from Eq. (14), which should apply when only one inertial layer is present. A striking feature is the very sharp stability boundary close to $q_{\min} = 1$. Results from the compressible FAR code are also shown in Fig. 4. At zero beta, the sound waves no longer propagate in a compressible formulation, and the inertial enhancement factor $M \simeq 1$ (as opposed to $M \simeq 1+2q^2$ when the sound waves propagate faster than the mode grows). Thus, the compressible and incompressible growth rates should and do differ by the factor $\sqrt{(1+2q^2)} = \sqrt{3}$.

The spatial dependence of the radial displacement eigenfunction is shown in Fig. 5 for various values of $q_{\min}$. The transition from one inertial layer, when $q_{\min} = 0.99$, to two separate layers, when $q_{\min} \lesssim 0.97$, is apparent. In the cases with two distinct layers, the ratios of the constant values for the eigenfunction in $[0, r_1]$ and $[r_1, r_2]$ are in good agreement with the analytic prediction in Eq. (25). Figure 6 shows the variation of growth rate with aspect ratio for this case with $q_{\min} = 1.0$, again with close agreement between analytic and computed results.

The nonmonotonic class of profiles studied here includes a marginally stable equilibrium (for ideal MHD modes). This remains true when finite resistivity is introduced and will be demonstrated for JET-like equilibria in Sect. 4.

Figure 7 shows a comparison of analytic [Eq. (13)] and computed growth rates as functions of beta, for the nonmonotonic $q(r) = 1+\Delta q[1-(r/r_1)^2]^2$ with $\Delta q = 0.1$, $r_1 = 0.33$, and an aspect ratio $A = 10$. In this case, the term in δW that is linear in beta is weakly stabilizing but is rapidly dominated by the quadratic term as beta is increased. Thereafter, the growth rate γ scales as $\beta^{4/3}$.

The remarkable quantitative agreement found in the foregoing comparisons demonstrates that the analytic, large-aspect-ratio theory provides an extremely valuable framework for understanding the varied scalings of linear growth rate with S, β, ϵ, etc., which emerge when different equilibrium $q(r)$ profiles are investigated.

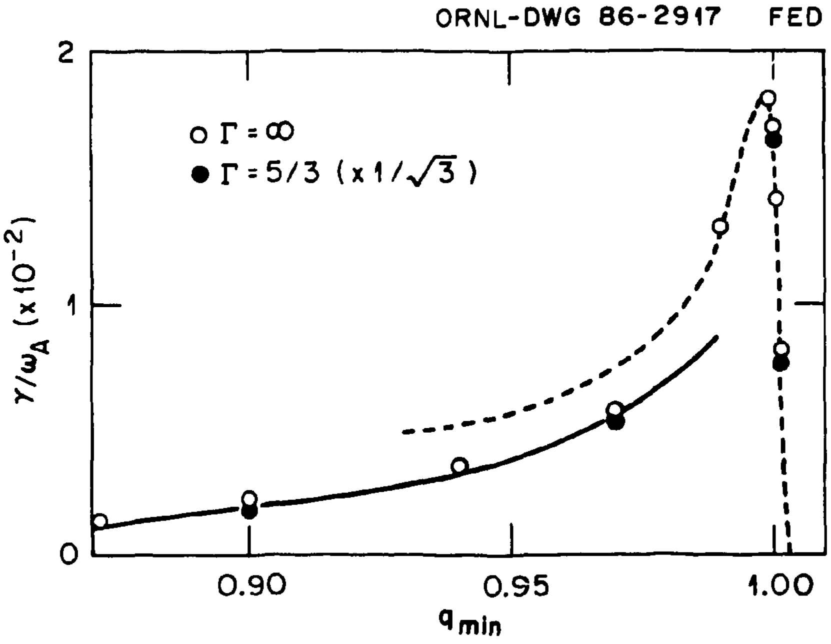

Fig. 4. Comparison of analytic and computed ideal growth rates for the non-monotonic safety factor $q(r) = q_{\min} + 0.2(1 - 4r^2)^2$, plotted against minimum value of q. The dashed curve is calculated from Eq. (14) (appropriate for a single inertial layer), the solid curve from Eq. (24) (appropriate for two distinct layers). Solid circles were computed using the compressible FAR code (and corrected by the factor $1\sqrt{3}$, see text). Open circles were computed using the incompressible code. $A = 10$, $\beta_0 = 0$.

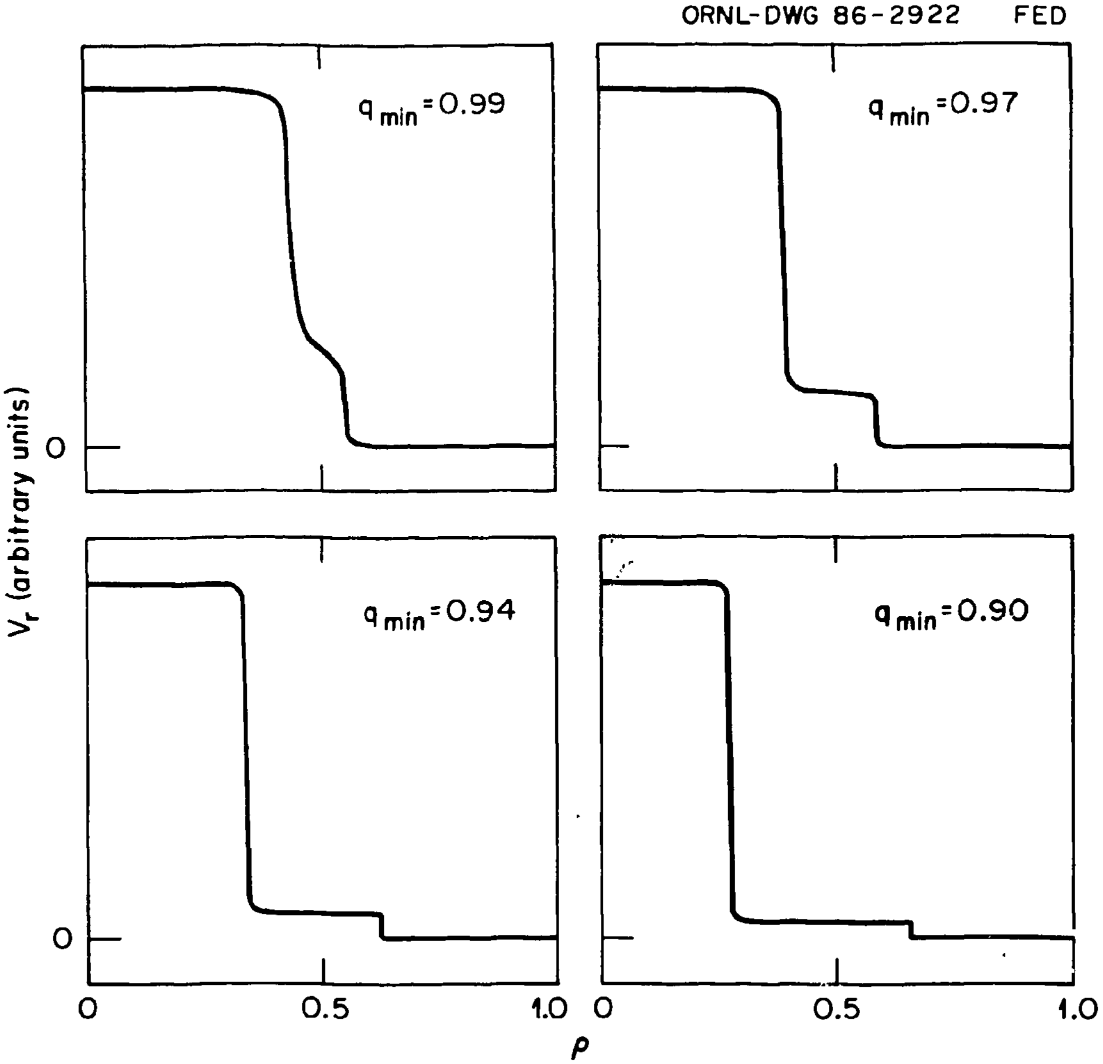

Fig. 5. Structure of the eigenfunction ($m = 1$ component of radial velocity) as a function of radius, for various values of q_{min}. $A = 10$, $\beta_0 = 0$, $q = q_{min} + 0.2(1 - 4r^2)^2$.

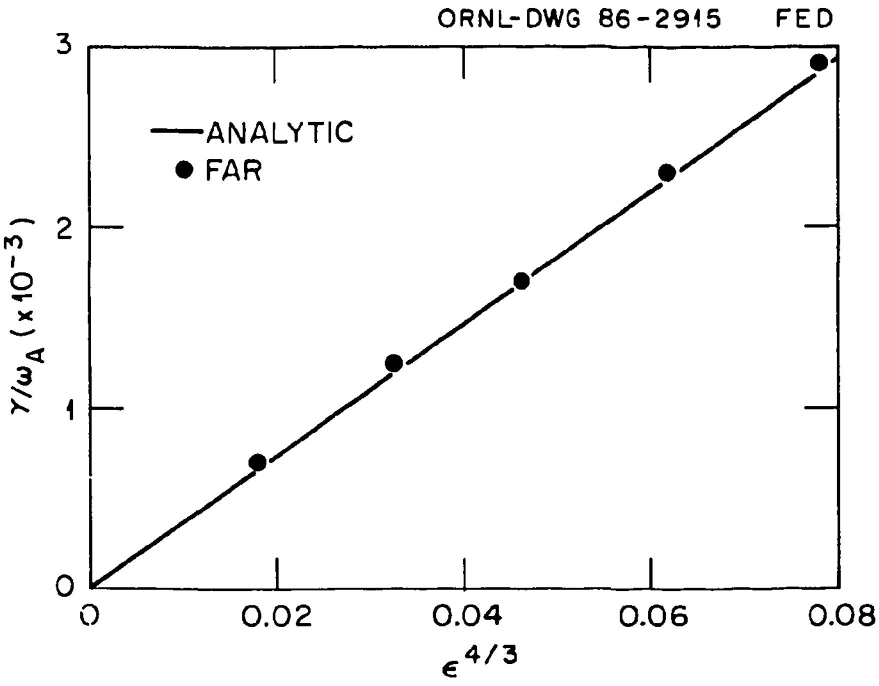

Fig. 6. Ideal growth rate vs inverse aspect ratio $\epsilon = A^{-1}$, for the equilibrium of Figs. 4 and 5. $q_{\min} = 1.0$. Analytic results (solid curve) are from Eq. (13).

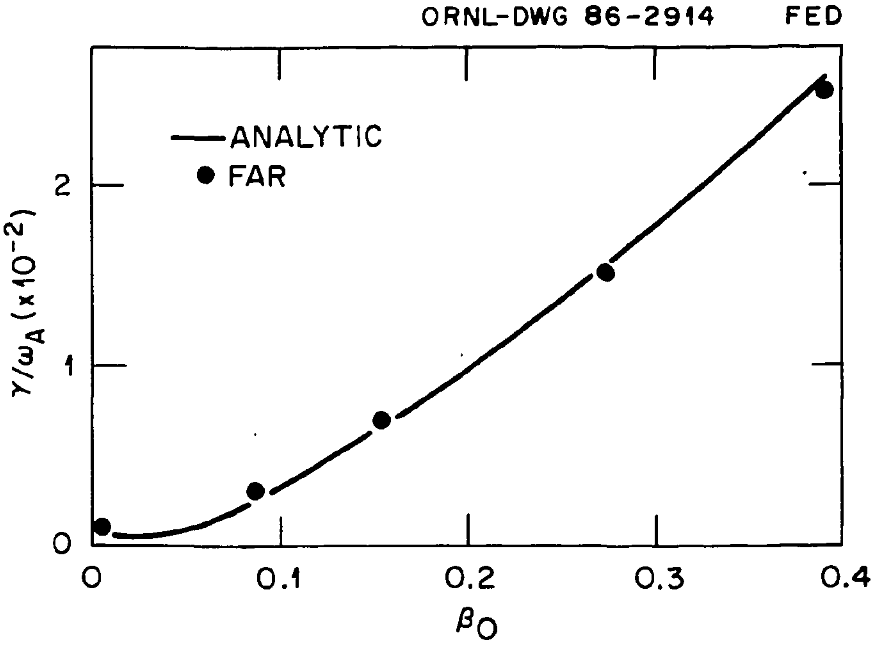

Fig. 7. Growth rate plotted vs β_0, peak value of beta. Analytic results (solid line) are from Eq. (13). $A = 10$, $q = 1 + 0.1(1 - 9r^2)^2$, $p = p_0[q - \Psi/\Psi(a)]^2$ with $\Psi = \int_0^r R_0 B_\theta dr$.

4. NUMERICAL RESULTS

In this section we extend the results of Sect. 3 by computing growth rates of ideal and resistive MHD modes in various equilibria for which the analytic theory should be expected to break down; namely, equilibria of small aspect ratio ($A < 3$), strongly shaped cross section, very flat $q(r)$ within $[0, r_1]$, or very low shear at the $q = 1$ surface.

Figure 8 shows the transition from resistive kink behavior $\left(\gamma \propto S^{-1/3}\right)$ to the more slowly growing tearing mode (reconnecting mode,[12] $\gamma \propto S^{-3/5}$) at high values of S, for the profile $q(r) = 0.9\left[1 + (r/0.65)^4\right]^{1/2}$ at $A = 1.4$. [We are forced to use this very tight aspect ratio to recover tearing mode behavior even for the high S values ($\sim 10^8$) used.] In the high-S, or tearing, regime, this mode should be sensitive to the stabilizing effect of favorable average curvatures.[24] This effect is, however, rather weak at the $q = 1$ surface, since the D_R of ref. 24 is much reduced there.

Figure 9 contrasts the resistive kink mode eigenfunction corresponding to Fig. 3 with the very localized tearing mode eigenfunction corresponding to Fig. 8 (at $S = 10^7$).

Figure 10 shows the growth rate of the $m = 1$ mode at the JET aspect ratio of $A = 2.5$ for the nonmonotonic $q(r) = q_{\min} + 0.1\left(1 - 8r^2 + 16r^4\right)$ and several values of S. The equilibria in this case have a circular boundary. The behavior of γ is qualitatively the same as that found at large aspect ratio (Fig. 4), and a notable feature is again the sharp stability boundary. In this case, when $q_{\min} \geq 1$, the growth rates are almost independent of S, with very weak resistive damping when $q_{\min} > 1$ (Fig. 11). As noted in the previous section, this shows that the non-monotonic profile considered is marginally stable to both ideal and resistive $m = 1$ instability when $q_{\min}$ is slighly above unity. For $q_{\min} < 1$, the usual $\gamma \propto S^{-1/3}$ scaling of resistive kink modes is also displayed in Fig. 11.

Figure 12 shows the destabilizing effect of beta for the previous case with $q_{\min} = 1$, while Fig. 13 shows a new important *destabilizing* effect from triangular shaping. This last result is in qualitative agreement with analytic theory. Previous results[22] have indicated that triangular, quadrangular, and high-order shaping is stabilizing for internal kink modes, but in these calculations monotonic $q(r)$ was assumed.

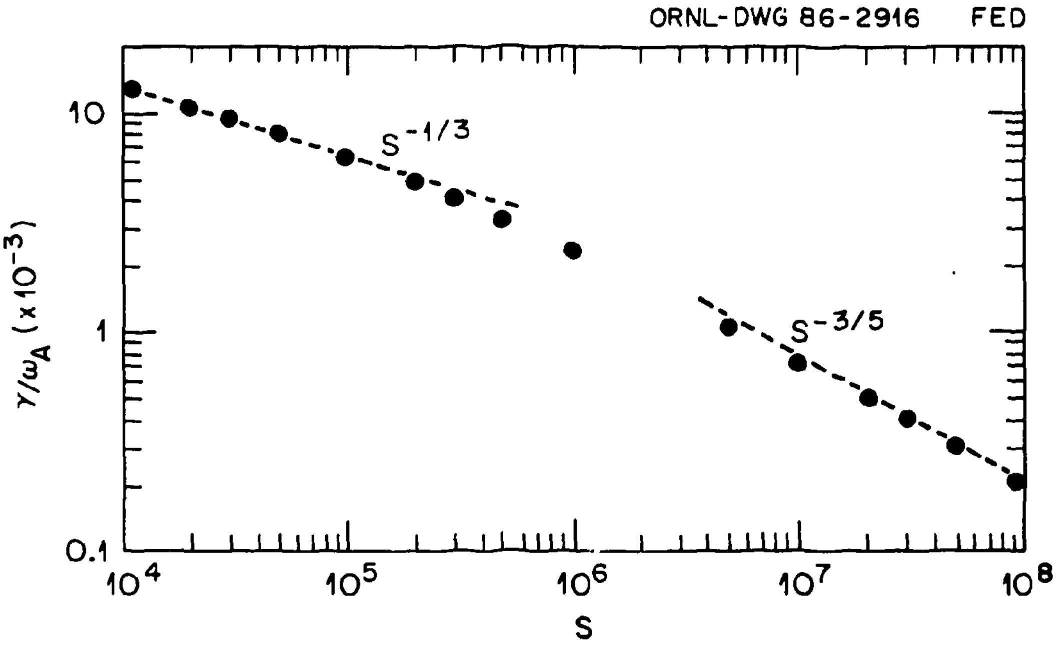

Fig. 8. Computed growth rate of $m = 1$ kink mode as a function of magnetic Reynolds number S. $A = 1.4$, $\beta_0 = 0$, $q = 0.9[1 + (r/0.65)^4]^{1/2}$.

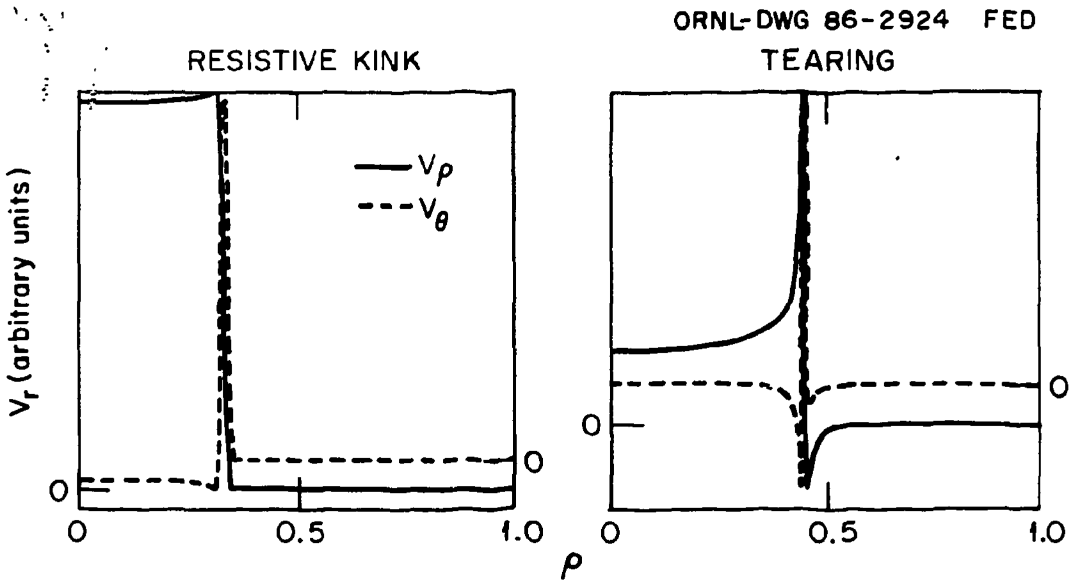

Fig. 9. Eigenfunction $V_r(r)$ for the resistive kink mode $[A = 10^2, \beta_0 = 0, q = 0.9(1 + r^2), S = 10^7]$ and $m = 1$ reconnecting mode $\{A = 1.4, \beta_0 = 0, q = 0.9\ [1 + (r/0.65)^4]^{1/2}, S = 10^7\}$.

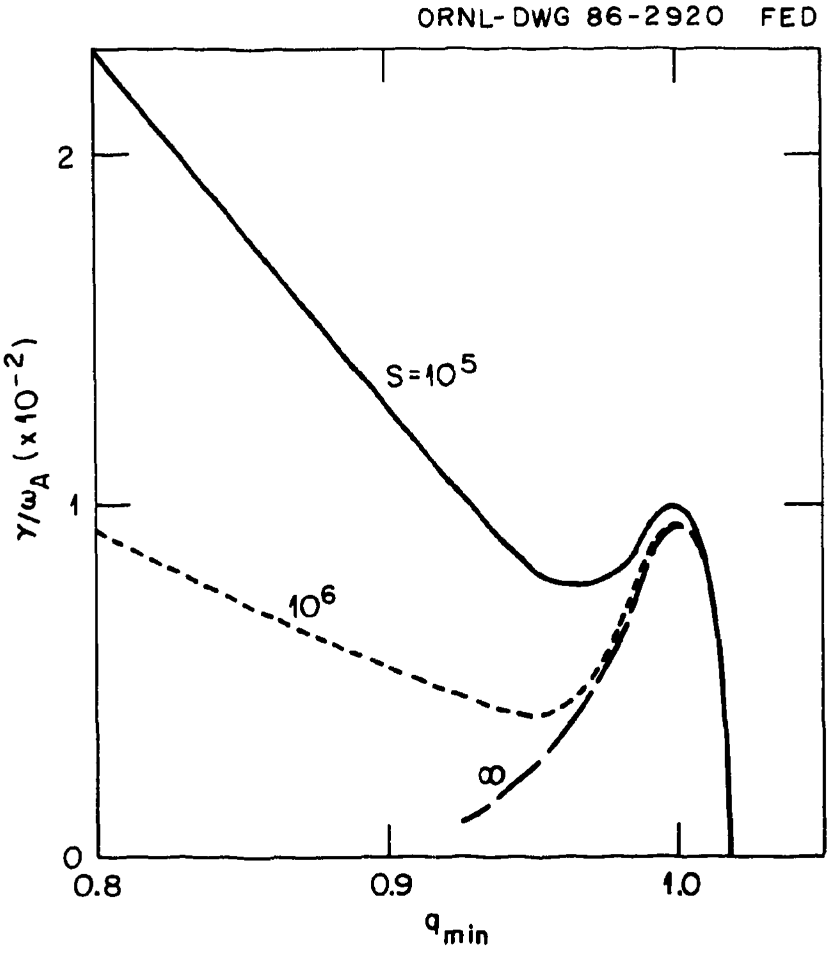

Fig. 10. Computed growth rates for $A = 2.5$, $\beta_0 = 0$, $q(r) = q_{min} + 0.1(1 - 8r^2 + 16r^4)$, and several values of S, plotted vs q_{min}.

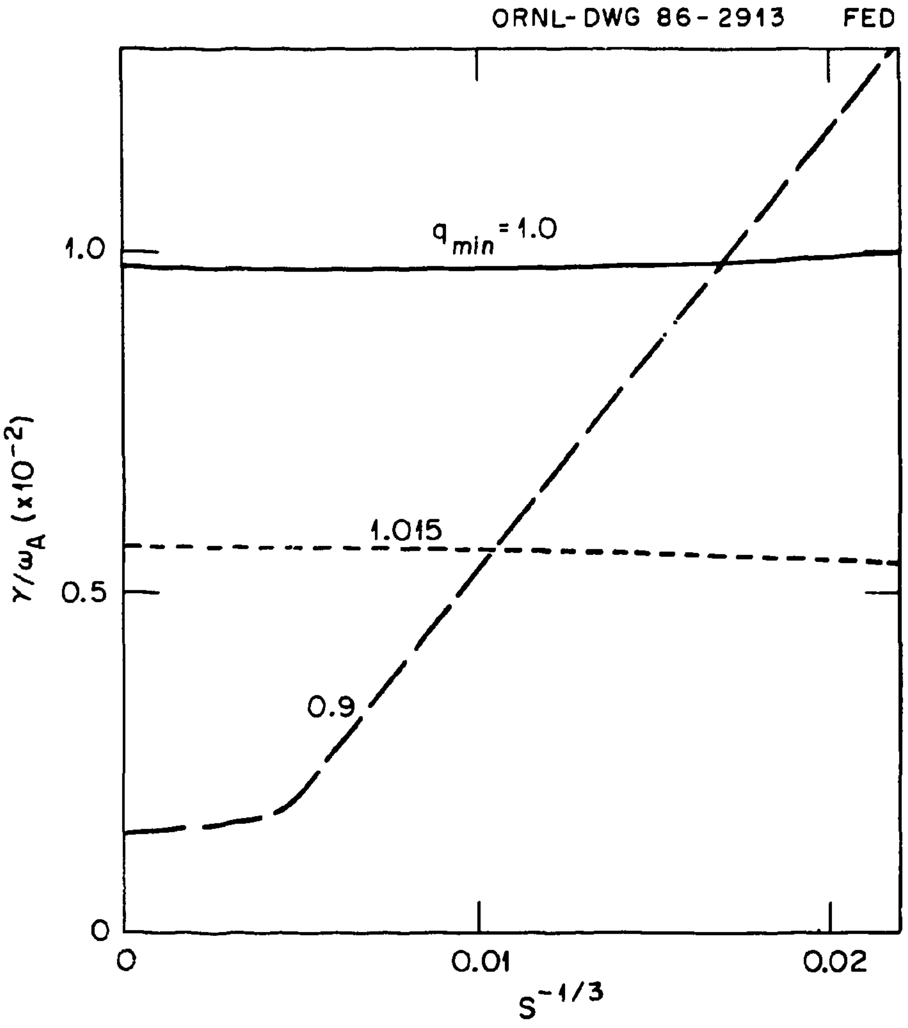

Fig. 11. Computed scaling of kink mode growth rates with S for three values of q_{min} and the equilibrium of Fig. 10.

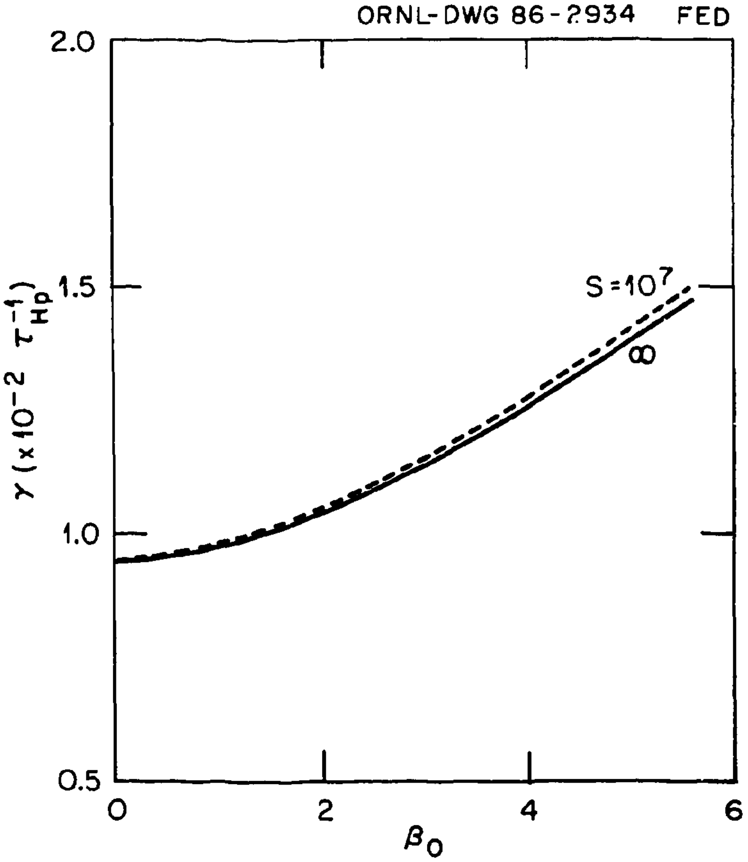

Fig. 12. **Computed growth rate as a function of β_0 for the equilibrium of Fig. 10 with $q_{min} = 1.0$.**

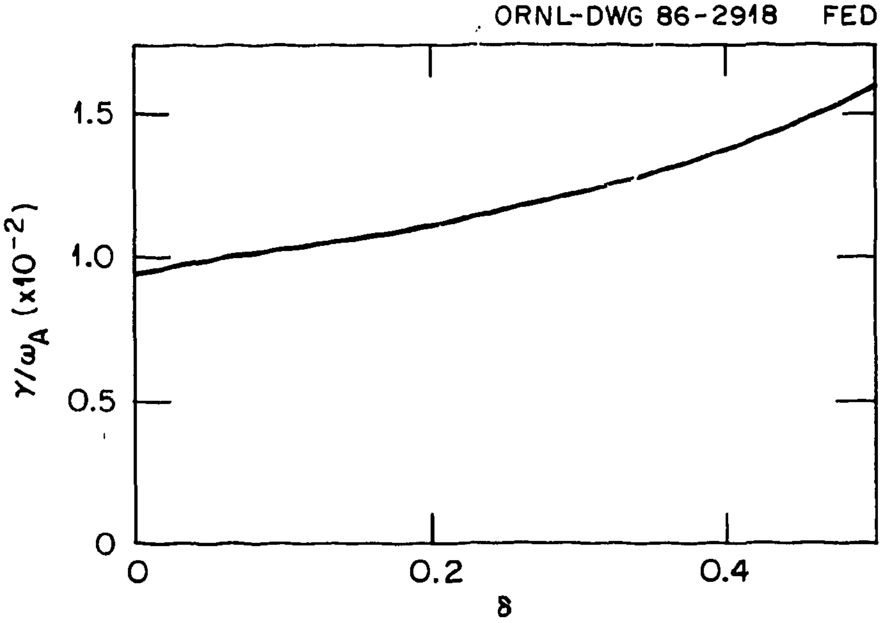

Fig. 13. Computed growth rate as a function of triangularity of the plasma boundary for the equilibrium of Fig. 10 with $\beta_0 = 0$, $q_{\min} = 1.0$.

The present result shows that this stabilizing effect is profile-dependent and can be reversed for nonmonotonic $q(r)$.

Recently, Wesson[7] has suggested a sawtooth model that is quite different from the original Kadomtsev model and has as its crux the assumption of an "ultra-flat" $q(r)$ profile for $0 < r \leq r_1$. This assumption is supported both by the measurements on ASDEX[20] and by transport code simulations, which, once such a flat q is established, tend to show very small deviations from it. Figure 14 shows the growth rate as a function of q on axis for an "ultra-flat" profile,

$$q = q_0 \left[1 + \left(\frac{r}{0.462}\right)^{12}\right]^{1/6} ,$$

at the JET aspect ratio $A = 2.5$ for a central beta of 2%. Various values of S are shown, but it is clear that the unstable mode is essentially ideal near $q_0 \sim 1$. For $q_0 \geq 1.02$, the $m = 2$ tearing mode becomes unstable: the transition from an $m = 1$ to an $m = 2$ mode is clear in the energy spectra of the eigenmodes. The sharp ideal stability boundary similar to that found for nonmonotonic $q(r)$ is again evident. Growth rates calculated from the compressible FAR code are also shown in Fig. 14. For this finite beta, equilibrium sound propagation along the magnetic field is faster than mode growth, so that the compressible and incompressible results are in good quantitative agreement.

In Fig. 15 the dependence of the linear growth on beta is shown for the case in Fig. 14 ($S = 10^6$), and in Fig. 16 the eigenfunctions are compared for various values of β_0 and q_0. In all cases, the eigenfunctions extend out to a significant radius; in addition, those closest to marginal stability show the rounded feature observed in the experimentally reconstructed flows using soft X-ray data.[26]

Figure 17 shows a similar plot of γ vs q_0 for a somewhat less flat profile,

$$q(r) = q_0 \left[1 + \left(\frac{r}{0.46}\right)^{4}\right]^{1/2} ,$$

with all other parameters identical to Fig. 14. The increasingly sharp ideal stability boundary as the shear within the $q = 1$ radius decreases is evident when Figs. 14 and 17 are compared.

Experimental measurements on TEXTOR[21] have produced evidence of somewhat different profiles of the safety factor and longitudinal current. In TEXTOR, measurements of the poloidal magnetic field indicate an axial value of the safety

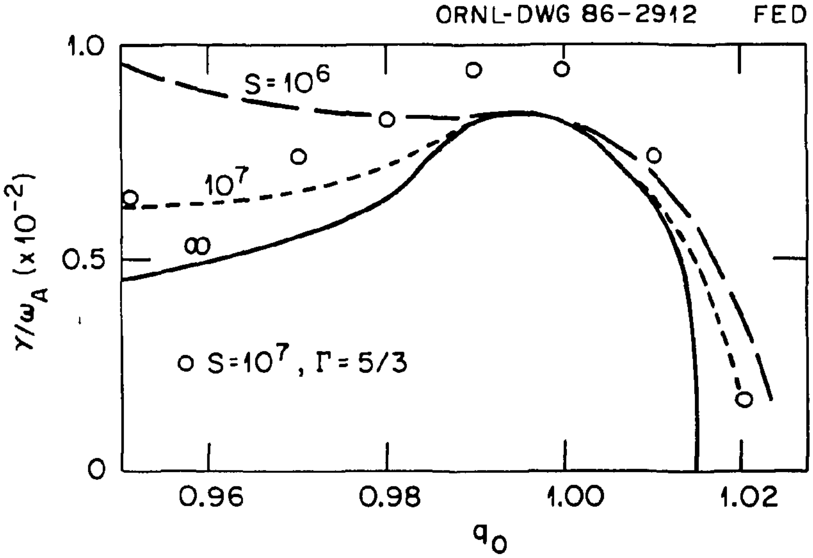

Fig. 14. Computed growth rate as a function of q_0, for $A = 2.5$, $\beta_0 = 2\%$, $q = q_0[1 + (r/0.462)^{12}]^{1/6}$, $p(r) = p_0(1 - \Psi/\Psi_a)^2$, and various values of S. Open circles are growth rates obtained using the compressible FAR code at $S = 10^7$.

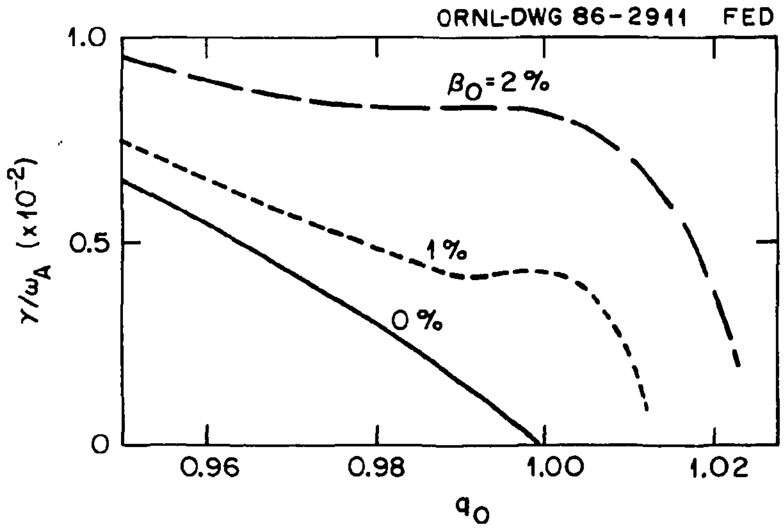

Fig. 15. Computed growth rate as a function of q_0 for various values of β_0 and the equilibrium of Fig. 14. $S = 10^6$.

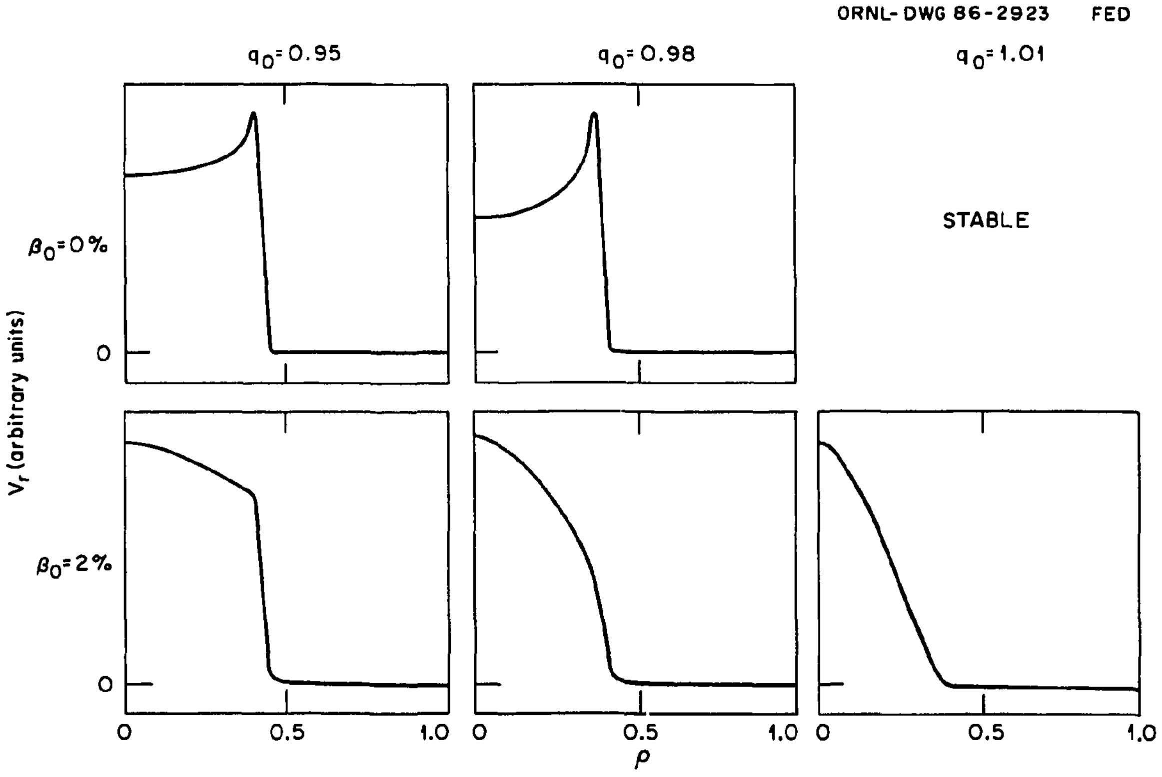

Fig. 16. Comparison of $m = 1$ eigenfunctions, $V_r(r)$ for various values of β_0 and q_0 and the equilibrium of Fig. 14. $S = 10^6$.

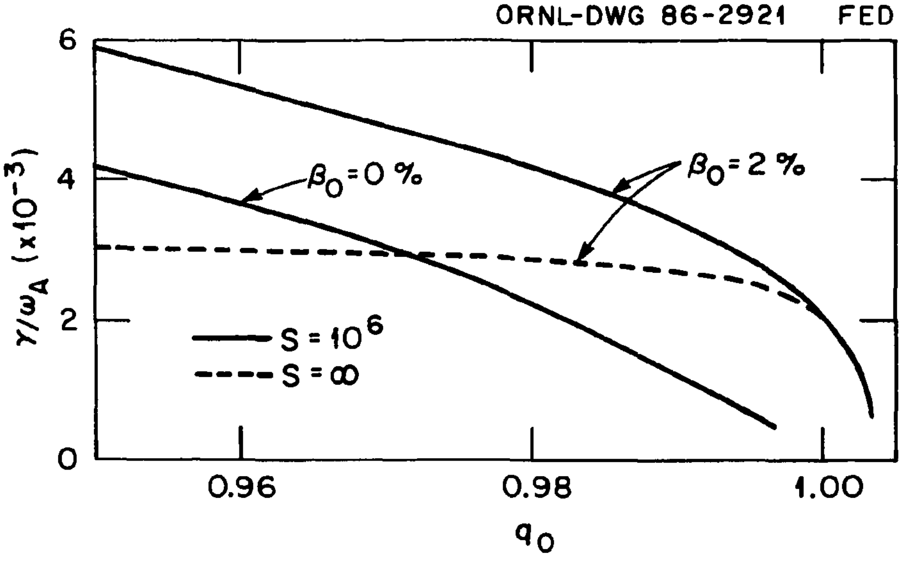

Fig. 17. Computed growth rates of $m = 1$ kink mode for $A = 2.5$, $q(r) = q_0[1 + (r/0.46)^4]^{1/2}$, $p = p_0(1 - \Psi/\Psi_a)^2$, and various values of β_0 and S.

factor $q_0 \leq 0.7$, with a point of inflection in the current $J_{\|}(r)$ and somewhat reduced shear at the $q = 1$ surface. For such an equilibrium, the original theory of Bussac et al. for ideal[8] and resistive[10] stability is valid. This theory predicts that, at large aspect ratio, the ideal MHD mode should be stable below some critical beta values, while the resistive $m = 1$ mode should be unstable (whatever the beta).

Since the effective Δ' for driving the resistive $m = 1$ mode in toroidal geometry[10] is $[q'(r_1)]^2 / \left(\epsilon_1^2 \delta W^T\right)$ for a large-aspect-ratio device, it is of interest to investigate what might be gained by modifying the current profile to remove the shear completely at r_1 $[q'(r_1) \to 0]$ in a tight-aspect-ratio torus. To study the general properties of profiles of this class, we adopt the simple parameterization

$$q = 0.6 + 2.2r^2 - 2.2\left(r^2 - r_1^2\right) \exp\left[-100(r^2 - r_1^2)^2\right] \ ,$$

with $r_1 = 0.426$ so that

$$q'(r_1) = q''(r_1) = 0$$

with $q(r_1) = 1$.

Results from the FAR code for this equilibrium profile (with $\beta \equiv 0$) are shown in Fig. 18, where a strong stabilizing trend is evident as A is reduced. Surprisingly, for a force-free equilibrium, the mode becomes overstable at small aspect ratio. Overstability may (as in the favorable curvature stabilization[24] of conventional tearing modes) be symptomatic of a stabilizing mechanism within the layer, which could yield absolute stability below some critical value of A. This is difficult to establish computationally and remains a conjecture.

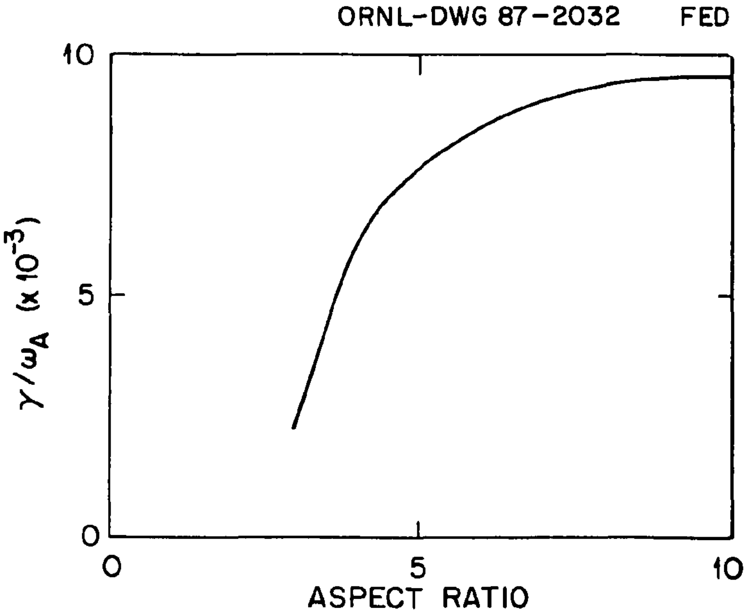

Fig. 18. Computed growth rate of $m = 1$ kink mode for $\beta_0 = 0$, $q(r) = 0.6 + 2.2r^2 - 2.2(r^2 - r_1^2)\exp[-100(r^2 - r_1^2)]$, $r_1 = 0.426$, and $S = 10^6$, plotted vs aspect ratio A. The mode becomes overstable at the smallest aspect ratio shown.

5. DISCUSSION AND CONCLUSIONS

A key ingredient in understanding, and possibly controlling, internal disruptions in tokamaks is an understanding of the stability boundary that is crossed at the instant of the fast temperature crash. An important clue is provided by the experimental observation that the phase inversion radius of the temperature collapse, which is usually interpreted as the radius of the $q = 1$ surface, is not small. The marginal $q(r)$ profiles therefore appear to pass through, or close to, unity at a finite distance r_1 from the axis of the discharge.

As a result of the calculations presented here, we can distinguish three distinct classes of $q(r)$ profile that possess this property and can be marginally stable to $m = 1$ modes:

1. nonmonotonic $q(r)$ with a minimum value close to unity at $r = r_1$,
2. ASDEX-like, or ultra-flat, $q(r)$ profiles that are close to unity over the whole region $[0, r_1]$,
3. monotonic $q(r)$ profiles for which q_0 is well below unity, $q(r_1) = 1$, and r_1 is a point of inflection for q, or at least a point of weak shear.

Examples of these profiles have been analyzed for ideal and resistive growth close to marginal stability, and earlier analytic theory[8] has been extended to provide a framework for understanding computational results from the initial value code FAR. Remarkable agreement has also been found in comparing analytic and computed growth rates.

Among the new results presented here are the following observations.

- Very sharp stability boundaries can be found when a critical q value determines stability. Examples are given for "ultra-flat" and non-monotonic q profiles.
- $S^{-1/3}$ scaling of linear growth rates is not found close to marginal stability for any of the three classes of profiles just described.
- Triangular shaping of the plasma cross section can be destabilizing. Its effect is dependent on the $q(r)$ profile.
- Equilibria with axial q values well below unity have been found and may be stable to resistive as well as ideal MHD $m = 1$ modes, in a tight-aspect-ratio torus. Overstability of the mode makes the determination of a stability boundary in A difficult.

Many of the features of the sawtooth in smaller tokamaks were explained by the model of Jahns et al.,[27] which invoked island growth of the resistive kink mode. In particular, the precursor oscillations and their growth rates agreed with the model proposed. In larger tokamaks, such as JET, however, precursor oscillations are not usually observed[28] in conditions of constant current. In addition, the initial plasma displacement in the sawtooth collapse is too fast (100 μs in JET)[28] for the model of ref. 27. This suggests that the steep, ideal MHD, stability boundaries apparent in Figs. 4 and 10 might be involved. We can calculate the initial time dependence to be expected as an equilibrium evolves resistively through such a boundary. Assuming a time dependence of the q profile such that

$$q = q(r)\left(1 - \frac{t}{\tau_\eta}\right) ,$$

with

$$\tau_\eta = \frac{r_1^2}{\eta c^2} ,$$

and using Eq. (14) for the growth rate [for a nonmonotonic $q(r)$ with $(q_{\min} - 1) = \delta q$], we find that the mode growth is initially given by $\exp(t/\tau_H)^{3/2}$, with the hybrid time τ_H defined by

$$\tau_H \simeq \left(3{\tau_A}^2\tau_\eta/\delta q_c\right)^{1/3} , \tag{26}$$

where δq_c is the value of δq at the stability boundary. Thus, even though the mode is an ideal MHD instability, the resistive evolution of q introduces $\eta^{1/3}$ into the time scale. Estimating this hybrid growth time for JET parameters, we find $\tau_H \sim 300$ μs, which is still a little too long to account for the experimental observations. To understand the fast time scales involved, it therefore appears that theory must look to nonlinear, or kinetic theory, phenomena.

To understand the nature of the internal disruptions in tokamaks, it is necessary to study the *nonlinear* evolution of the $m = 1$, $n = 1$ kink mode. The present paper suggests a number of equilibrium $q(r)$ profiles that could be marginally stable in linear studies. Because of the considerable differences in these q profiles, a wide variety of nonlinear behavior is to be expected, with the classic Kadomtsev reconnection as one possibility. Such studies are under way using a nonlinear version of the FAR code and will form the basis of a future paper.

REFERENCES

1. B. B. Kadomtsev, *Sov. J. Plasma Phys.* **1**, 389 (1975).
2. B. B. Kadomtsev, p. 555 in *Plasma Physics and Controlled Nuclear Fusion Research 1976* (*Proc. 6th Int. Conf. Berchtesgaden, 1976*), Vol. 1, IAEA, Vienna, 1977.
3. V. V. Parail and G. V Pereversev, *Sov. J. Plasma Phys.* **6**, 14 (1980).
4. W. Pfeiffer, *Nucl. Fusion* **25**, 673 (1985).
5. A. Sykes and J. A. Wesson, *Phys. Rev. Lett.* **37**, 140 (1976).
6. B. V. Waddell, M. N. Rosenbluth, D. A. Monticello, and R. B. White, *Nucl. Fusion* **16**, 528 (1976).
7. J. A. Wesson, *Plasma Phys. Controlled Nucl. Fusion* **28**, 243 (1986).
8. M. N. Bussac, R. Pellat, D. Edery, and J. L. Soulé, *Phys. Rev. Lett.* **35**, 1638 (1975).
9. B. Coppi, R. Galvao, R. Pellat, M. N. Rosenbluth, and P. H. Rutherford, Sov. *J. Plasma Phys.* **2**, 533 (1976).
10. M. N. Bussac, D. Edery, R. Pellat, and J. L. Soulé, p. 607 in *Plasma Physics and Controlled Nuclear Fusion Research* (*Proc. 6th Int. Conf. Berchtesgaden, 1976*), Vol. 1, IAEA, Vienna, 1977.
11. B. Basu and B. Coppi, *Nucl. Fusion* **17**, 1245 (1977).
12. G. Ara et al., *Ann. Phys. (N.Y.)* **112**, 443 (1978).
13. R. E. Denton, J. F. Drake, and R. G. Kleva, UMLPF 86–004, Univ. Maryland, 1985.
14. R. E. Denton, J. F. Drake, R. G. Kleva, and D. A. Boyd, UMLPF 86–016, Univ. Maryland, 1985.
15. J. W. Connor and R. J. Hastie, CLM–M106, Culham Laboratory, Abingdon, England, 1985.
16. L. E. Zakharov, *Sov. J. Plasma Phys.* **4**, 503 (1978).
17. A. B. Mikhailovskii, *Sov. J. Plasma Phys.* **9**, 190 (1983).

18. L. A. Charlton, J. A. Holmes, H. R. Hicks, V. E. Lynch, and B. A. Carreras, *J. Comput. Phys.* **63**, 107 (1986).

19. T. C. Hender, R. J. Hastie, and D. C. Robinson, submitted to *Nucl. Fusion.*

20. K. McCormick et al., p. 199 in *Controlled Fusion and Plasma Physics* (*Proc. 12th European Conf. Budapest, 1985)*, Vol. 1, European Phys. Soc., Budapest, 1985.

21. H. Soltwich, W. Stodiek, A. Kaleck, and J. Schlüter, DOE/CH/03073-T26, U.S. DOE, 1985.

22. D. Edery, G. Laval, R. Pellat, and J. L. Soulé, *Phys. Fluids* **19**, 260 (1976).

23. I. B. Bernstein, E. A. Freeman, M. D. Kruskal, and R. M. Kulsrud, *Proc. R. Soc. London Ser. A* **244**, 17 (1958).

24. A. H. Glasser, J. M. Greene, and J. L. Johnson, *Phys. Fluids* **18**, 875 (1975).

25. J. A. Holmes, B. A. Carreras, H. R. Hicks, V. E. Lynch, and K. E. Rothe, *Phys. Fluids* **25**, 800 (1982).

26. P. Kirby, F. Nave, and J. A. Wesson, paper presented at the 11th International Conference on Plasma Physics and Controlled Nuclear Fusion Research, Kyoto, Japan, November 1986. Proceedings to be published.

27. G. L. Jahns, M. Soler, B. V. Waddell, J. D. Callen, and H. R. Hicks, *Nucl. Fusion* **19**, 609 (1978).

28. D. J. Campbell et al., *Nucl. Fusion* **26**, 1085 (1986).

APPENDIX

The ideal MHD theory of Bussac et al.[1] can be readily extended to the case with two distinct radii at which q is unity. Denoting these by r_1 and r_2, we follow refs. 1 and 2 in expanding the ideal energy integral δW in powers of the inverse aspect ratio, for a large-aspect-ratio equilibrium with circular plasma cross section and poloidal beta of order unity. Using the straight-field-line coordinates of refs. 1 and 2, (r, θ, Φ),

$$r^2 = 2R_0 \int_0^{\psi} \frac{q}{I} \, d\Psi \ , \tag{A.1}$$

$$\theta = \frac{I}{q} \int_0^{\ell} \frac{d\ell}{R^2 B_p} \ , \tag{A.2}$$

and ϕ is the axisymmetric angle. In Eqs. (A.1) and (A.2), Ψ is the poloidal flux function, the magnetic field is given by

$$\underset{\sim}{B} = \nabla\Psi \times \nabla\phi + I(\Psi)\nabla\phi \ ,$$

and ℓ measures arc length along $\underset{\sim}{B}$.

In lowest order of the aspect ratio expansion, one finds $\delta W_0 = 0$, provided ξ_0 is chosen to satisfy

$$\frac{\partial}{\partial r}\left(r\xi_{r0}\right) + \frac{\partial}{\partial\theta}\xi_{\theta 0} = 0 \ , \tag{A.3}$$

where $\underset{\sim}{\xi}_0 \propto e^{i(m\theta - n\phi)}$ with $m = n = 1$.

In second order, $\underset{\sim}{\xi}_1$ is also required to satisfy Eq. (A.3) and

$$\delta W_2 = 2\pi^2 R_0 B_0^2 \int r \, dr \left[\left(\frac{1}{q} - 1 \right)^2 \left| r \frac{d\xi_{r0}}{dr} \right|^2 \right] \ . \tag{A.4}$$

This is minimized by the choice

$$\xi_{r0} = \begin{cases} \xi_0, \ 0 \leq r < r_1 \\ \bar{\xi}_0, \ r_1 < r < r_2 \\ 0, \ r_2 < r \leq a \end{cases} \tag{A.5}$$

when $\delta W_2 = 0$. The relative magnitudes of the "top-hat" solutions ξ_0 and $\bar{\xi}_0$ are arbitrary at this stage.

In fourth order, after minimizing with respect to $\underset{\sim}{\xi}_2$, the second-order correction to the $m = 1$ component, and with respect to the $m = 0$ part of $\underset{\sim}{\xi}_1$, one obtains

$$\delta W_4 = \delta W_4\left(0, r_1\right) + \delta W_4\left(r_1, r_2\right) + \delta W_4\left(r_2, a\right) \ ,$$

where

$$\begin{aligned}\frac{\delta W_4\left(0, r_1\right)}{2\pi^2 R_0 B_0^2} = \xi_0^2 \frac{r_1^4}{R^2} & \left[\frac{1}{2} s_1 - \frac{3}{4}\left(s_1 + \beta_{p1}\right)^2 - \frac{9}{8}\left(s_1 + \beta_{p1}\right) + \frac{9}{64}\right] \\ & + \frac{3}{2} \xi_0 \xi_1\left(r_1\right) \frac{r_1^3}{R}\left(s_1 + \beta_{p1} - \frac{1}{4}\right) + \frac{1}{4} r_1^3 \xi_1 \xi_1' \bigg|_{r_1} \ ,\end{aligned} \tag{A.6}$$

$$\begin{aligned}\frac{\delta W_4\left(r_1, r_2\right)}{2\pi^2 R_0 B_0^2} = \bar{\xi}_0^2 \frac{r_2^4}{R^2} & \left[\frac{1}{2} s_2 - \frac{3}{4}\left(s_2 + \beta_{p2}\right)^2 - \frac{9}{8}\left(s_2 + \beta_{p2}\right) + \frac{9}{64}\right] \\ & - \bar{\xi}_0^2 \frac{r_1^4}{R^2}\left[\frac{1}{2} s_1 - \frac{3}{4}\left(s_1 + \beta_{p1}\right)^2 - \frac{9}{8}\left(s_1 + \beta_{p1}\right) + \frac{9}{64}\right] \\ & + \frac{3}{2} \frac{r_2^3}{R} \bar{\xi}_0 \bar{\xi}_1\left(r_2\right)\left(s_2 + \beta_{p2} - \frac{1}{4}\right) - \frac{3}{2} \frac{r_1^3}{R} \bar{\xi}_0 \bar{\xi}_1\left(r_1\right) \\ & \times\left(s_1 + \beta_{p1} - \frac{1}{4}\right) + \frac{1}{4} r_2^3 \bar{\xi}_1 \bar{\xi}_1' \bigg|_{r_2} - \frac{1}{4} r_1^3 \bar{\xi}_1 \bar{\xi}_1' \bigg|_{r_1} \ ,\end{aligned} \tag{A.7}$$

$$\frac{\delta W_4\left(r_2, a\right)}{2\pi^2 R_0 B_0^2} = -\frac{1}{4} r_2^3 \tilde{\xi}_1 \tilde{\xi}_1' \bigg|_{r_2} \ . \tag{A.8}$$

Here

$$s_j = \int_0^{r_j} \frac{r^3 dr}{r_j^4}\left(\frac{1}{q^2} - 1\right) \ , \qquad j = 1, 2 \ ,$$

$$\beta_{pj} = \frac{2}{B_p^2\left(r_j\right)} \int_0^{r_j} dr\left(-\frac{dp}{dr}\right) \frac{r^2}{r_j^2} \ , \qquad j = 1, 2 \ ,$$

and $\xi_1(r)$, $\bar{\xi}_1(r)$, $\tilde{\xi}_1(r)$ are all solutions of the homogeneous, $m = 2$ Euler equation,

$$\frac{d}{dr}\left[r^3\left(\frac{1}{q} - \frac{1}{2}\right)^2 \frac{d\xi_1}{dr}\right] - 3r\left(\frac{1}{q} - \frac{1}{2}\right)^2 \xi_1 = 0 \ . \tag{A.9}$$

Since the full $m = 2$ solutions in the three regions are given by

$$\xi^{(m=2)} = \begin{cases} \xi_1(r) - \xi_0\left(\Delta' + \frac{1}{2} \frac{r}{R}\right) & \text{in } [0, r_1] \\ \bar{\xi}_1(r) - \bar{\xi}_0\left(\Delta' + \frac{1}{2} \frac{r}{R}\right) & \text{in } [r_1, r_2] \ , \\ \tilde{\xi}_1(r) & \text{in } [r_2, a] \end{cases}$$

continuity of $\xi^{(m=2)}$ requires that

$$\xi_1(r_1) - \xi_0 \left(\Delta' + \frac{1}{2}\frac{r}{R}\right)_{r_1} = \bar{\xi}_1(r_1) - \bar{\xi}_0 \left(\Delta' + \frac{1}{2}\frac{r}{R}\right)_{r_1} \tag{A.10}$$

and

$$\tilde{\xi}_1(r_2) = \bar{\xi}_1(r_2) - \bar{\xi}_0 \left(\Delta' + \frac{1}{2}\frac{r}{R}\right)_{r_2} . \tag{A.11}$$

In addition, $\xi_1(r)$ must be regular as $r \to 0$, and $\xi(r)$ must be small at the $q = 2$ surface if that falls within the plasma, or $\tilde{\xi}_1(a)$ must vanish if $q_a < 2$.

In these equations, $\Delta(r)$ is the Shafranov shift, so that

$$\Delta'(r_1) = \frac{r_1}{R}\left(s_1 + \beta_{p1} + \frac{1}{4}\right) ,$$

$$\Delta'(r_2) = \frac{r_2}{R}\left(s_2 + \beta_{p2} + \frac{1}{4}\right) .$$

To proceed with the minimization of δW_4, we choose to represent $\bar{\xi}_1(r)$, which is a solution of Eq. (A.9), by a linear superposition of $\xi_1(r)$ and $\tilde{\xi}_1(r)$, the solutions for which are regular at $r = 0$ and at the $q = 2$ surface.

Thus, writing

$$\bar{\xi}_1(r) = \alpha\xi_1(r) + \beta\tilde{\xi}_1(r) ,$$

the two continuity relations (A.10) and (A.11) are used to eliminate α and β. The energy integral may now be expressed in terms of ξ_0, $\bar{\xi}_0$, and two quantities characterizing the magnitude of the $\xi_1(r)$ and $\tilde{\xi}_1(r)$ solution [$\xi_1(r)$ and $\tilde{\xi}_1(r_2)$, say], together with six quantities that characterize the solutions ξ_1 and $\tilde{\xi}_1$,

$$b = \frac{r_1\xi'(r_1)}{\xi_1(r_1)} \qquad c = \frac{r_2\xi_1'(r_2)}{\xi_1(r_2)} \qquad d = \frac{r_1\tilde{\xi}_1'(r_1)}{\tilde{\xi}_1(r_1)}$$

$$e = \frac{r_2\tilde{\xi}_1'(r_2)}{\tilde{\xi}_1(r_2)} \qquad f = \frac{\tilde{\xi}_1(r_1)}{\tilde{\xi}_1(r_2)} \qquad g = \frac{\xi_1(r_2)}{\xi_1(r_1)} .$$

Thus

$$\delta W_4 = \delta W_4\left[\xi_0,\ \bar{\xi}_0 \cdot \xi_1(r_1),\ \tilde{\xi}_1(r_2);\ b,\ c,\ d,\ e,\ f,\ g,\ s_j,\ \beta_{pj}\right] .$$

The next step is to minimize δW_4 with respect to ξ_1 and $\tilde{\xi}_1$. These minimizations are algebraic but tediously complicated. The final result is

$$\begin{aligned}\delta W_4 = 2\pi^2 R\, B_0^2 \bigg[& \left(\xi_0 - \overline{\xi}_0\right)^2 \frac{r_1^4}{R^2}\, \delta W_1 + \overline{\xi}_0^2 \frac{r_2^4}{R^2}\, \delta W_2 \\ & + \overline{\xi}_0 \left(\xi_0 - \overline{\xi}_0\right) \frac{r_1^4}{R^2}\, \delta W_3 \bigg] \ ,\end{aligned} \tag{A.12}$$

with

$$\begin{aligned}\delta W_1 = \frac{1}{4} \bigg\{ & 2s_1 + (b+3)\,(\beta_{p1} + s_1)^2 + \frac{3}{2}\,(b-1)\,(\beta_{p1} + s_1) + \frac{9}{16}\,(b-1) \\ & - \frac{1}{\alpha}\frac{(e-c)}{(d-b)} \left[(b+3)\,(s_1 + \beta_{p1}) + \frac{3}{4}\,(b-1) \right]^2 \bigg\} \ ,\end{aligned} \tag{A.13}$$

$$\begin{aligned}\delta W_2 = \frac{1}{4} \bigg\{ & 2s_2 - (e+3)\,(\beta_{p2} + s_2)^2\, [1 + (e+3)/\alpha] - \frac{3}{2}\,(e+3)\,(\beta_{p2} + s_2) \\ & \times [1 + (e-1)/\alpha] + \frac{9}{16}\,(1-e)\,[1 + (e-1)/\alpha] \bigg\} \ ,\end{aligned} \tag{A.14}$$

$$\begin{aligned}\delta W_3 = \frac{1}{2} \bigg\{ & 2s_1 - 3\,(\beta_{p1} + s_1) - \left[(e+3)\,(\beta_{p2} + s_2) + \frac{3}{4}\,(e-1) \right] \bigg[(b+3)\,(\beta_{p1} + s_1) \\ & + \frac{3}{4}\,(b-1) \bigg] \frac{1}{2\alpha}\frac{r_2}{r_1} \frac{\left[(d-b)f + (e-c)g\, r_2^2/r_1^2 \right]}{(d-b)fg} \bigg\} \ ,\end{aligned} \tag{A.15}$$

$$\alpha = \frac{(e-c)fg}{(1-fg)} - \frac{1}{4}\frac{r_1^2}{r_2^2}\frac{(1-fg)}{(d-b)fg} \left[\frac{(d-b)f}{(1-fg)} + \frac{(e-c)g}{(1-fg)}\frac{r_2^2}{r_1^2} \right]^2 \ . \tag{A.16}$$

The necessary and sufficient condition for ideal MHD $m = 1$ stability can now be expressed as

$$\begin{aligned} & \delta W_1 > 0 \ , \\ & \delta W_3 > 0 \ , \\ & \left(\frac{r_2}{r_1}\right)^8 (\delta W_2)^2 - 4\delta W_1\ \delta W_3 < 0 \ . \end{aligned} \tag{A.17}$$

If any one of these three inequalities is violated, an ideal $m = 1$ mode is unstable.

The appropriate ideal growth rates and eigenfunctions of unstable modes are obtained by equating Eq. (A.1?) to the energy contributions from the two inertial layers at r_1 and r_2, in a way analogous to that discussed in the main text for a single inertial layer. The single-surface result [Eq. (11)] now becomes

$$\frac{\left(\xi_0 - \overline{\xi}_0\right)^2}{I_1(\gamma)} + \frac{\overline{\xi}_0^2}{I_2(\gamma)} = -\frac{\delta W_4\left(\xi_0, \overline{\xi}_0\right)}{\left(2\pi^2 R\, B_0^2\right)} , \qquad \text{(A.18)}$$

where

$$I_j(\gamma) = \int_{-\infty}^{\infty} \frac{dx}{3\gamma^2/\omega_A^2 + \left[q'\left(r_j\right)\right]^2 x^2} ,$$

and $\delta W_4\left(\xi_0, \overline{\xi}_0\right)$ is given by Eq. (A.12).

On solving for γ/ω_A and extremizing with respect to the ratio $\xi_0/\overline{\xi}_0$, we obtain the growth rates and eigenfunctions of the ideal modes. It is these results [Eqs. (24) and (25) of the main text] that have been used in the comparison of analytic growth rates with those obtained from the FAR code.

References

1. M. N. Bussac, R. Pellat, D. Edery, and J. L. Soulé, *Phys. Rev. Lett.* **35**, 1638 (1975).
2. A. B. Mikhailovskii, *Sov. J. Plasma Phys.* **4**, 503 (1978).

ORNL/TM-10331
Dist. Category UC-20 g

INTERNAL DISTRIBUTION

1. B A. Carreras
2. L. A. Charlton
3. R. A. Dory
4. R. H. Fowler
5. S. P. Hirshman
6. J. A. Holmes
7. D. A. Spong
8. W. I. van Rij
9. G. E. Whitesides
10–11. Laboratory Records Department
12. Laboratory Records, ORNL-RC
13. Document Reference Section
14. Central Research Library
15. Fusion Energy Division Library
16–17. Fusion Energy Division Publications Office
18. ORNL Patent Office

EXTERNAL DISTRIBUTION

19. R. J. Hastie, Culham Laboratory, Abingdon, Oxon OX14 3DB, England
20. T. C. Hender, Culham Laboratory, Abingdon, Oxon OX14 3DB, England
21. P. H. Diamond, Institute for Fusion Studies, University of Texas at Austin, Austin, TX 78712
22. Office of the Assistant Manager for Energy Research and Development, Department of Energy, Oak Ridge Operations Office, P.O. Box E, Oak Ridge, TN 37831
23. J. D. Callen, Department of Nuclear Engineering, University of Wisconsin, Madison, WI 53706
24. R. W. Conn, Department of Chemical, Nuclear, and Thermal Engineering, University of California, Los Angeles, CA 90024
25. S. O. Dean, Director, Fusion Energy Development, Science Applications International Corp., Gaithersburg, MD 20760
26. H. K. Forsen, Bechtel Group, Inc., Research Engineering, P.O. Box 3965, San Francisco, CA 94205
27. J. R. Gilleland, GA Technologies, Inc., Fusion and Advanced Technology, P.O. Box 85608, San Diego, CA 92138
28. R. W. Gould, Department of Applied Physics, California Institute of Technology, Pasadena, CA 91125
29. R. W. Gross, Plasma Research Library, Columbia University, New York, NY 10027
30. D. M. Meade, Princeton Plasma Physics Laboratory, P.O. Box 451, Princeton, NJ 08544
31. W. M. Stacey, School of Mechanical Engineering, Georgia Institute of Technology, Atlanta, GA 30332
32. D. Steiner, Rensselaer Polytechnic Institute, Troy, NY 12181
33. R. Varma, Physical Research Laboratory, Navrangpura, Ahmedabad 380009, India
34. Bibliothek, Max-Planck Institut fur Plasmaphysik, D-8046 Garching bei Munchen, Federal Republic of Germany
35. Bibliothek, Institut fur Plasmaphysik, KFA, Postfach 1913, D-5170 Julich, Federal Republic of Germany

36. Bibliotheque, Centre de Recherches en Physique des Plasmas, 21 Avenue des Bains, 1007 Lausanne, Switzerland
37. Bibliotheque, Service du Confinement des Plasmas, CEA, B.P. No. 6, 92 Fontenay-aux-Roses (Seine), France
38. Documentation S.I.G.N., Department de la Phy [illegible] Plasma et de la Fusion Controlee, Centre d'Etudes Nucleaires, [illegible] Centre du Tri, 38081 Cedex, Grenoble, France
39. Library, Culham Laboratory, UKAEA, Abingc [illegible] .ordshire, OX14 3DB, England
40. Library, FOM-Instituut voor Plasma-Fysica, Rijnhuizen, Edisonbaan 14, 3439 MN Nieuwegein, The Netherlands
41. Library, Institute of Plasma Physics, Nagoya University, Nagoya, Japan
42. Library, International Centre for Theoretical Physics, Trieste, Italy
43. Library, Laboratorio Gas Ionizatti, CP 56, I-00044 Frascati (Roma), Italy
44. Library, Plasma Physics Laboratory, Kyoto University, Gokasho, Uji, Kyoto, Japan
45. Plasma Research Laboratory, Australian National University, P.O. Box 4, Canberra, A.C.T. 2000, Australia
46. Thermonuclear Library, Japan Atomic Energy Research Institute, Tokai, Naka, Ibaraki, Japan
47. G. A. Eliseev, I. V. Kurchatov Institute of Atomic Energy, P.O. Box 3402, 123182 Moscow, U.S.S.R.
48. V. A. Glukhikh, Scientific-Research Institute of Electro-Physical Apparatus, 188631 Leningrad, U.S.S.R.
49. I. Shpigel, Institute of General Physics, U.S.S.R. Academy of Sciences, Ulitsa Vavilova 38, Moscow, U.S.S.R.
50. D. D. Ryutov, Institute of Nuclear Physics, Siberian Branch of the Academy of Sciences of the U.S.S.R., Sovetskaya St. 5, 630090 Novosibirsk, U.S.S.R.
51. V. T. Tolok, Kharkov Physical-Technical Institute, Academical St. 1, 310108 Kharkov, U.S.S.R.
52. Library, Institute of Physics, Academia Sinica, Beijing, Peoples Republic of China
53. J. F. Clarke, Associate Director for Fusion Energy, Office of Fusion Energy, ER-50, Germantown, U.S. Department of Energy, Washington, DC 20545
54. D. B. Nelson, Division of Applied Plasma Physics, Office of Fusion Energy, Office of Energy Research, ER-54, Germantown, U.S. Department of Energy, Washington, DC 20545
55. N. A. Davies, Tokamak Systems Branch, Office of Fusion Energy, Office of Energy Research, ER-55, Germantown, U.S. Department of Energy, Washington, DC 20545
56. E. Oktay, Tokamak Systems Branch, Office of Fusion Energy, Office of Energy Research, ER-55, Germantown, U.S. Department of Energy, Washington, DC 20545
57. Theory Department Read File, c/o D. W. Ross, University of Texas, Institute for Fusion Studies, Austin, TX 78712
58. Theory Department Read File, c/o R. C. Davidson, Director, Plasma Fusion Center, NW 16-202, Massachusetts Institute of Technology, Cambridge, MA 02139
59. Theory Department Read File, c/o F. W. Perkins, Princeton Plasma Physics Laboratory, P.O. Box 451, Princeton, NJ 08544

60. Theory Department Read File, c/o L. Kovrizhnykh, Institute of General Physics, Academy of Sciences of the U.S.S.R., Ulitsa Vavilova 38, Moscow, U.S.S.R.
61. Theory Department Read File, c/o B. B. Kadomtsev, I. V. Kurchatov Institute of Atomic Energy, P.O. Box 3402, 123182 Moscow, U.S.S.R.
62. Theory Department Read File, c/o T. Kamimura, Institute of Plasma Physics, Nagoya University, Nagoya, Japan
63. Theory Department Read File, c/o C. Mercier, Euratom-CEA, Service de Recherches sur la Fusion Controlee, Fontenay-aux-Roses (Seine), France
64. Theory Department Read File, c/o T. E. Stringer, JET Joint Undertaking, Culham Laboratory, Abingdon, Oxfordshire OX14 3DB, England
65. Theory Department Read File, c/o K. Roberts, Culham Laboratory, Abingdon, Oxfordshire OX14 3DB, England
66. Theory Department Read File, c/o D. Biskamp, Max-Planck-Institut fur Plasmaphysik, D-8046 Garching bei Munchen, Federal Republic of Germany
67. Theory Department Read File, c/o T. Takeda, Japan Atomic Energy Research Institute, Tokai, Naka, Ibaraki, Japan
68. Theory Department Read File, c/o C. S. Liu, GA Technologies, Inc., P.O. Box 81608, San Diego, CA 92138
69. Theory Department Read File, c/o L. D. Pearlstein, Lawrence Livermore National Laboratory, P.O. Box 808, Livermore, CA 94550
70. Theory Department Read File, c/o R. Gerwin, CTR Division, Los Alamos National Laboratory, P.O. Box 1663, Los Alamos, NM 87545
71. R. E. Mickens, Department of Physics, Atlanta University, Atlanta, GA 30314
72. C. De Palo, Library, Associazione EURATOM-ENEA sulla Fusione, CP 65, I-00044 Frascati (Roma), Italy

73–228. Given distribution as shown in TIC–4500, Magnetic Fusion Energy (Category Distribution UC–20 g: Theoretical Plasma Physics)